and untreated mice was resected and fixed with 10% formalin. Paraffin-embedded samples were sliced into 3 μM sections for *hematoxylin and eosin* staining and immunostaining. Antibodies against α-smooth muscle actin (SMA) (DAKO, Glostrup, Denmark) were used to identify the pericyte and anti-CD31 (Abcam, MA, USA, USA), endothelial cell marker and anti-Ki67 (Labvision, Fremont, CA, USA) antibodies to recognise the growth state cells (G1, S, and M phase). Vascular areas within the tumours were measured as the index of tumour vascularity by stained with anti-CD31. Five fields of tumour sections were analysed at low magnification using a computerised image analyser (Image-Pro Plus, Media Cybernetics, MA, USA). The ratio of vessel area against tumour area without necrosis was calculated.

Statistical analysis

Values were expressed as the mean ± s.d. A two-tailed Student's *t*-test was used comparison between the pre- and post-treatment groups. ANOVA analysis, followed by Dunnett's test, was used for multi-group comparisons. Pearson's correlation coefficients were used for determination between a significant positive and negative relationship. Correlations between 0.4 and 0.6 were considered moderate, whereas correlations from 0.7 to 1.0 were considered strong. Significant differences were accepted when the *P*-value was below 0.05.

RESULTS

Figure 1A shows change of the Gd concentrations in DCE-MRI acquisition using Gd-DTPA at pretreatment, at 3-h, and 24-h post-injection of A-83-01. A progressive accumulation of Gd in the tumour was observed during the first 60 s followed by a plateau phase. The group treated with a single injection of A-83-01 showed the highest accumulation at 3 h post-injection of A-83-01 (1.7-fold the IAUGC$_{60}$, Figure 1B) associated with a larger s.d., and a similar level to those with pretreatment at 24 h (0.9-fold the IAUGC$_{60}$). At 24 h after repeated injection, the tumour accumulation increased a similar level to that at 3 h after the single injection (1.8-fold the IAUGC$_{60}$). Next, we observed changes of the tumour vasculature repeat-treated by A-83-01 using Gd-L. The Gd concentration in DCE-MRI acquisition of untreated mice was very low (Figure 1C). The Gd concentration with Gd-L in repeat-treated mice increased during the first 200 s, and reached the same plateau value as with that of the Gd-DTPA repeat-treated mice. Eventually the repeated A-83-01 treatment increased 3.8-fold the IAUGC$_{60}$ of Gd-L (Figure 1D), indicating a dramatic improvement in liposomal contrast agent delivery to the tumour.

From the data obtained above, v_p and K^{trans} values were calculated (Figure 2). With Gd-DTPA at 3 h after the single treatment, v_p and K^{trans} were high values accompanied with great variability, whereas at 24 h, v_p and K^{trans} were similar to those of the respective pretreatment values, suggesting that A-83-01 induced a transient change in the vasculature at around 3 h. On the other hand, at 24 h after repeated treatment, all mice showed increased v_p and K^{trans} with Gd-DTPA ($P < 0.05$) and Gd-L. At 3 h after the first treatment, v_p and K^{trans} did not show significantly elevated values with Gd-DTPA, therefore, it can be concluded that the repeated administration schedule changed the tumour state positively for better liposomal contrast-agent distribution. The most characteristic point of the v_p and K^{trans} changes was the large dispersion of v_p and K^{trans} values after repeated A-83-01 treatments with the use of Gd-L. The diversity of local permeability of treated tumours may lead to large

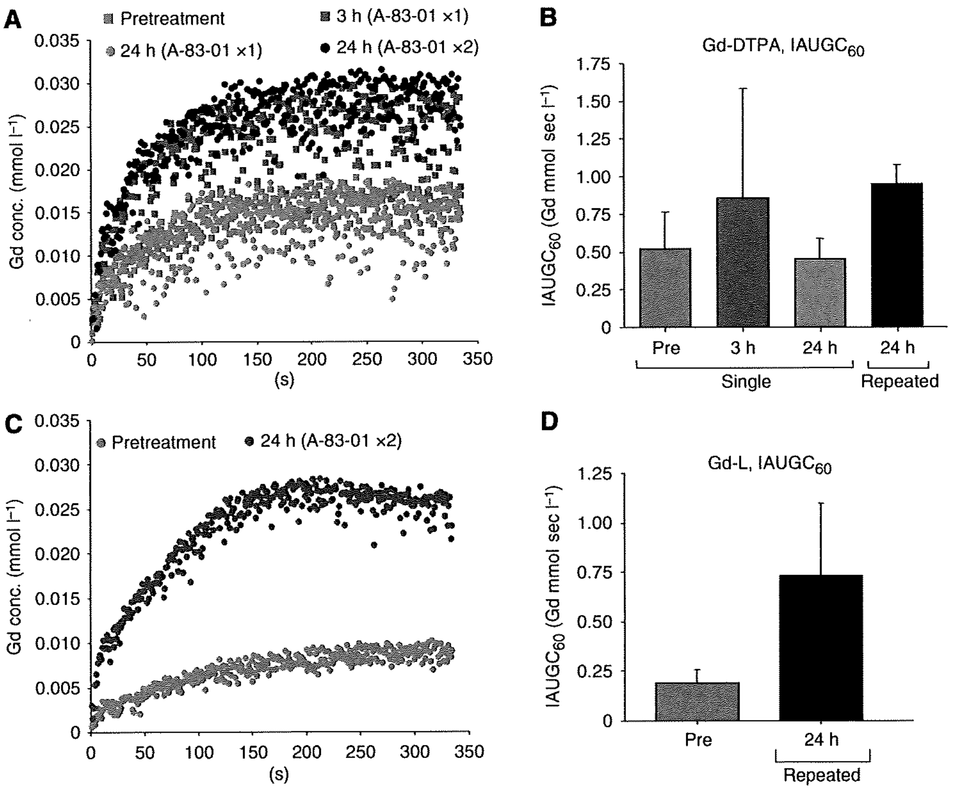

Figure 1 Mean gadolinium (Gd) uptake curves from regions-of-interest (ROI) over the whole tumour before (pre) and at different time points after (post) intraperitoneal A-83-01 injection with Gd-DTPA (**A**) and Gd-L (**C**), and IAUGC60$_{0-60}$ with Gd-DTPA (**B**) and Gd-L (**D**). Data points (**B**, **D**) indicate mean ± s.d. (N = 3–6).

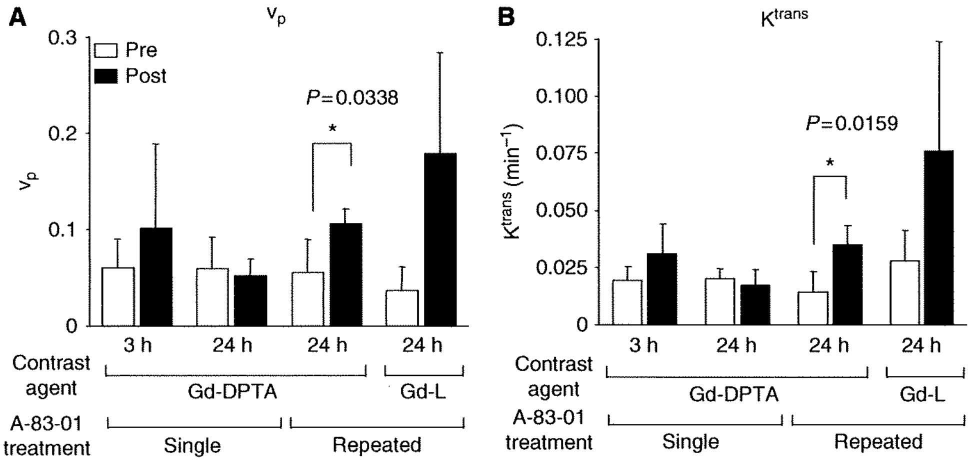

Figure 2 Values of fractional plasma volume (v_p) (**A**) and volume transfer constant (K^{trans}) (**B**) in the tumour before (pre) and at 3 h and 24 h after (post) single or repeated A-83-01 injections using gadolinium (Gd)-DTPA and Gd-L as a contrast agent. Each column represents the mean ± SD (N = 3 to 6).

dispersion of Gd-L. The mouse tumour core showed an increase in the Gd concentration, as shown in Figure 1C, whereas the tumour rim showed a high peak concentration at about 1 min post-injection of Gd-L that then decayed (data not shown). In contrast, Gd-DTPA increased tumour Gd concentration homogeneously. This finding suggests that Gd-L could detect small changes in tumour micro-environments and brought about a big dispersion of v_p and K^{trans} values among treated mice.

Figure 3 shows histological observations of the tumours with or without the repeated A-83-01 treatment. Two distinct changes were observed, although there was no difference in tumour cell shape or necrosis. The first was intra-tumoural bleeding, which was exclusively configured at the periphery of the A-83-01-treated tumours with 200–300 μm width and 100 μm depth (Figure 3A). The bleeding lesions were not accompanied with tissue oedema, suggesting minute rupture of tumour vessels. This means that hyper-permeability had not occurred. The localised bleeding state may correspond to the accumulation site of Gd-L. The second observation was morphological changes of the tumour vasculature. Abnormal blood vessels with irregular dilation were seen in the untreated tumours, whereas the vasculature in A-83-01-treated mice was smaller, and its shape was more round, suggesting the vascular normalisation (Figure 3A). Tumour vascularity, the percentage of vascular area (1.2%) in the treated tumours (post) was not significantly lower than in the untreated tumours (pre, 2.9%, $P > 0.05$), as the change was very diverse within a tumour (Figure 3D). The abnormal tumour vessels were not accompanied with pericytes, which were identified because of SMA reactivity (Figure 3B). It is interesting to note that the normalised vessels in tumours treated with A-83-01 were surrounded by pericytes (Figure 3B). The Ki67 index (58.5%) was significantly higher in the perivascular region of the A-83-01-treated tumours compared with the untreated tumours (41.4%, $P < 0.05$) (Figure 3C, E). These findings suggested that the repeated A-83-01 treatment allowed the recovery of blood flow during 24 h.

In the evaluation of *apparent diffusion coefficient* value, single-treated groups at 3 and 24 h did not show a difference compared with the pretreatment, but the repeat-treated group at 24 h showed a significant difference ($P < 0.01$, Figure 4). Alteration of extra- and intracellular fluid volume balance in repeat-administrated protocol may occur in the tumour because the diffusion rate of intracellular water is 1 order of magnitude smaller than that of the extracellular water (Van Zijl *et al*, 1991; Gass *et al*, 2001).

Next, the relation of DCE-MRI parameters with Gd-DTPA to tumour *apparent diffusion coefficient* was investigated (Figure 5). There was a moderately negative correlation between *the* $IAUGC_{60}$ (Figure 5A),K^{trans}(Figure 5B),v_p, *and apparent diffusion coefficient* (Figure 5C). This suggests that these parameters may be of value in the assessment of tumour behaviour.

DISCUSSION

In this study, effects of a TβR-I inhibitor was firstly evaluated by means of DCE-MRI with Gd-DTPA and Gd-L in mice bearing colon 26 tumours. The effect of A-83-01 exhibited high $IAUGC_{60}$, v_p, and K^{trans} values at 24 h after repeated treatment.

An increase in K^{trans} by the use of Gd-L could conceivably increase the permeability and surface area of the capillary endothelium. The K^{trans} value estimated with Gd-L ($K^{trans} = 0.076 \pm 0.048\ \text{min}^{-1}$) after the repeated A-83-01 treatment was higher to that with Gd-DTPA ($K^{trans} = 0.035 \pm 0.009\ \text{min}^{-1}$) (Figure 2B). Liposomal contrast agents are promising for characterising the tumour vascularity and the angiogenesis status through DCE-MRI method.

Anti-angiogenic agents such as anti-VEGF antibody and tyrosine kinase inhibitor were reported that decrease both K^{trans} and IAUGC (O'Connor *et al*, 2007; Bradley *et al*, 2008; Bradley *et al*, 2009), and the decrease in K^{trans} in solid tumours is concerned with the anti-tumour effect (Morgan *et al*, 2003; Marzola *et al*, 2004; Nakamura *et al*, 2006; Flaherty *et al*, 2008). In this study, K^{trans}, $IAUGC_{60}$, and v_p were increased significantly 24 h after the A-83-01 treatment. This increase may be explained by different treatment protocols, different tumour models, and the different signal inhibition between anti-angiogenic agent such as kinase inhibitor and TβR-I inhibitor. Similar to A-83-01-treated colon 26 solid tumours, LY364947-treated M109 solid tumours increased $IAUGC_{60}$ at 3 h and recovered fully by 24 h post-injection (Supplementary Figure S2).

It was reported that in a limited situation, anti-angiogenic agents work to deliver more drugs into tumours through the induction of vascular normalisation (Jain, 2001). Untreated colon 26 tumours showed low permeability, in spite of the absence of pericytes or the leaky vessel state (Figure 2B, 3B). The increased K^{trans} and $IAUGC_{60}$ values were related to the increased number of growth state cells around the tumour vessel, and were correlated to the decreased *apparent diffusion coefficient value*. Because of no significant difference in tumour cell shape after treatment (Figure 3A), intra-cellular volume did not change. Decreased *apparent diffusion coefficient*, therefore, reflected a decrease in

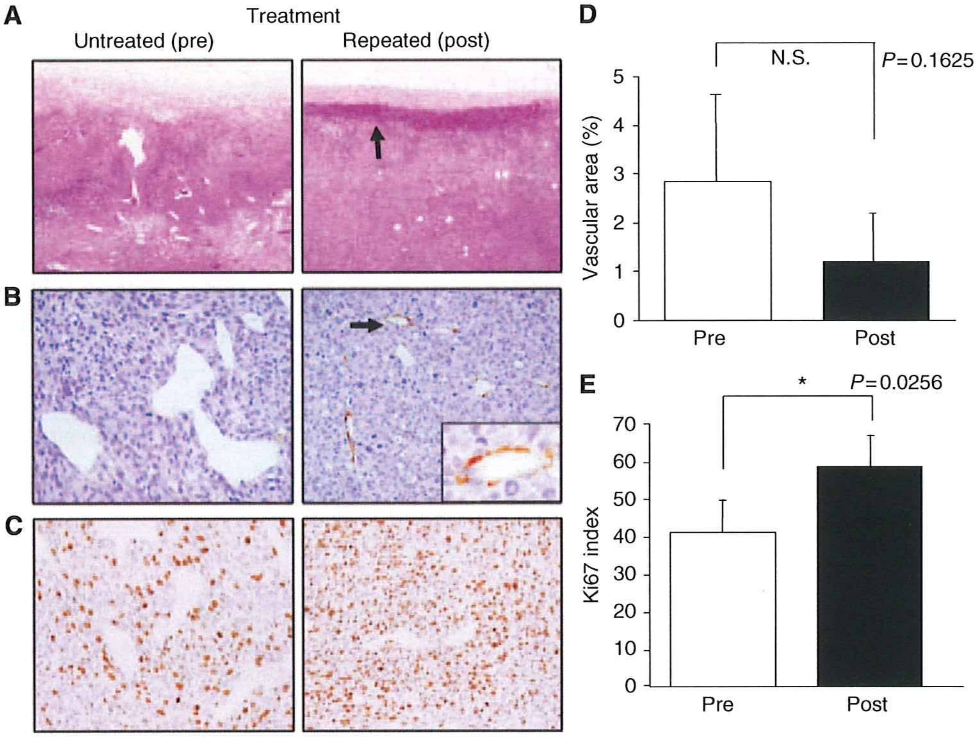

Figure 3 Histological analysis of tumours in untreated (pre) and treated (post) mice 24 h after repeated A-83-01 treatment. (**A**) *Hematoxylin and eosin* staining (× 40). Arrow indicates that zonal bleeding was observed at the periphery of the tumour with A-83-01 treatment. (**B**) Immunostaining with anti-smooth muscle actin (SMA) antibody (× 200 and inset, × 400). Irregularly dilated tumour vessels in untreated mice are not associated with pericytes, whereas the normalized vessels after A-83-01 treatment are surrounded by SMA-positive pericytes (arrow). (**C**) Immunostaining with Ki67. Ki67-positive proliferating tumour cells in the perivascular region are more prominent in the A-83-01 treated tumour than the untreated tumour (× 200). (**D**) Mean percentage of the vascular areas within the tumours as the index of tumour vascularity. (**E**) Ki67 index in perivascular regions of (**C**). Proliferating tumour cells were increased significantly in A-83-01 treated tumours compared with untreated tumours ($P < 0.05$). Each column represents the mean ± s.d. ($N = 5$).

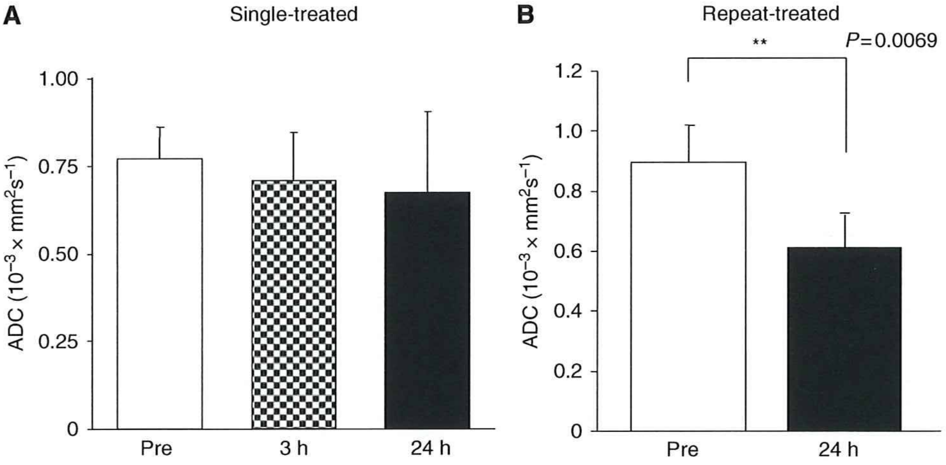

Figure 4 *Apparent diffusion coefficient* of the tumours before (pre) and at different time points after (post) single (**A**) and repeated (**B**) intraperitoneal A-83-01 injection. Repeat-treated tumours showed significant decreases in *apparent diffusion coefficient* compared with pretreatment. Each column represents the mean ± s.d. ($N = 4$).

extra-cellular fluid, suggesting that the recovery of delivery may be related to vessel normalisation.

Furthermore, similar to negative correlation between tumour interstitial fluid pressure and permeability of tumour (Haider *et al*, 2007), IAUGC, K^{trans}, and v_p showed a moderate negative correlation to *apparent diffusion coefficient*, suggesting that these parameters may be providing similar information. As *apparent diffusion coefficient* is acquired in clinic widely to detect and diagnose a tumour, it could apply conveniently to examine the permeability of tumour in patients.

Although there is room for improvement, DCE-MRI using liposomal contrast agents such as Gd-L could be an important method to anticipate the extravasation of the liposomal anti-cancer drug during TβR-I inhibitor-combined therapy.

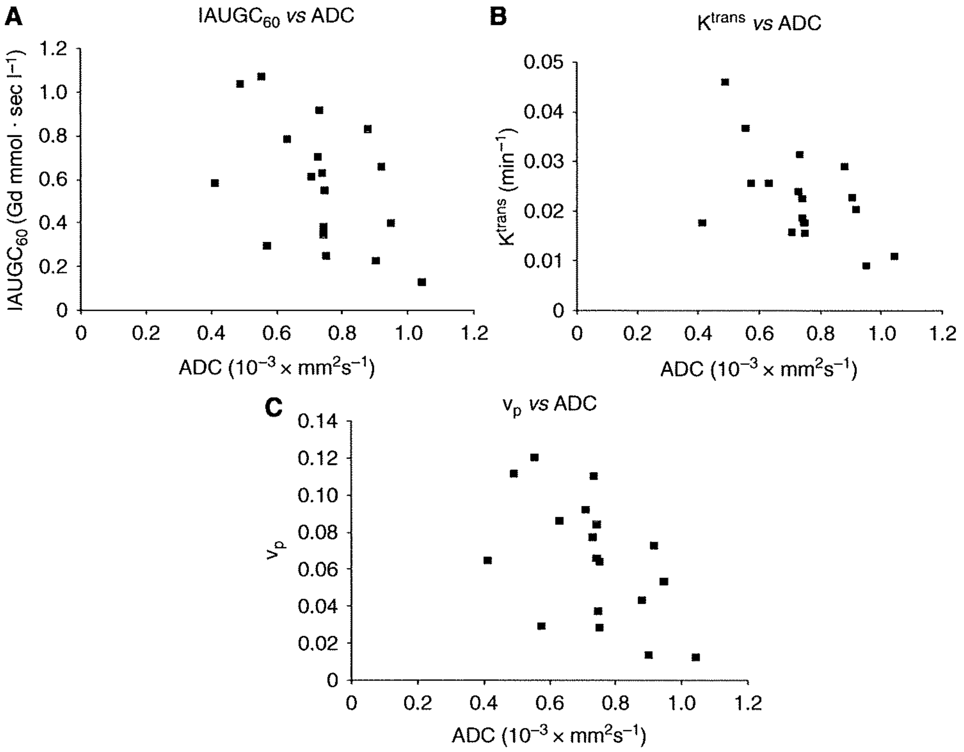

Figure 5 IAUGC$_{60}$, transfer constant volume transfer constant (K^{trans}), and fractional plasma volume (v_p) with gadolinium (Gd)-DTPA *vs* tumour *apparent diffusion coefficient* (*ADC*). There was a moderately negative correlation between the IAUGC$_{60}$ and ADC ($r = -0.4774$, $P = 0.0451$, $N = 18$) (**A**), between K^{trans} and ADC ($r = -0.5333$, $P = 0.0227$, $N = 18$) (**B**), and between v_p and ADC ($r = -0.5253$, $P = 0.0252$, $N = 18$) (**C**).

In summary, we found that DCE-MRI parameters, K^{trans}, IAUGC$_{60}$, and v_p were positively related to tumour vasculature by the treatment of A-83-01. Thus, TβR-I inhibitor has the potential to enhance the delivery of liposomal anti-cancer drugs and contrast agents. DCE-MRI forms a capable tool to determine the administration schedule of combination therapy with TβR-I inhibitor by K^{trans} and v_p quantitation.

ACKNOWLEDGEMENTS

This work was supported in part by a grant for research on Regulatory Science of Pharmaceuticals and Medical Devices from the Ministry of Health, Labor and Welfare of Japan and by the Open Research Center Project. Ms Y Taniguchi is acknowledged for providing many helpful comments, and Mr S Kawagoe and Mr T Nakamura for assistance.

REFERENCES

Bradley DP, Tessier JJ, Lacey T, Scott M, Jurgensmeier JM, Odedra R, Mills J, Kilburn L, Wedge SR (2009) Examining the acute effects of cediranib (RECENTIN, AZD2171) treatment in tumor models: a dynamic contrast-enhanced MRI study using gadopentate. *Magn Reson Imaging* **27**: 377–384

Bradley DP, Tessier JL, Checkley D, Kuribayashi H, Waterton JC, Kendrew J, Wedge SR (2008) Effects of AZD2171 and vandetanib (ZD6474, Zactima) on haemodynamic variables in an SW620 human colon tumour model: an investigation using dynamic contrast-enhanced MRI and the rapid clearance blood pool contrast agent, P792 (gadomelitol). *NMR Biomed* **21**: 42–52

Daldrup-Link HE, Okuhata Y, Wolfe A, Srivastav S, Oie S, Ferrara N, Cohen RL, Shames DM, Brasch RC (2004) Decrease in tumor apparent permeability-surface area product to a MRI macromolecular contrast medium following angiogenesis inhibition with correlations to cytotoxic drug accumulation. *Microcirculation* **11**: 387–396

Ewing JR, Knight RA, Nagaraja TN, Yee JS, Nagesh V, Whitton PA, Li L, Fenstermacher JD (2003) Patlak plots of Gd-DTPA MRI data yield blood-brain transfer constants concordant with those of 14C-sucrose in areas of blood-brain opening. *Magn Reson Med* **50**: 283–292

Flaherty KT, Rosen MA, Heitjan DF, Gallagher ML, Schwartz B, Schnall MD, O'Dwyer PJ (2008) Pilot study of DCE-MRI to predict progression-free survival with sorafenib therapy in renal cell carcinoma. *Cancer Biol Ther* **7**: 496–501

Gass A, Niendorf T, Hirsch JG (2001) Acute and chronic changes of the apparent diffusion coefficient in neurological disorders-biophysical mechanisms and possible underlying histopathology. *J Neurol Sci* **186**: S15–S23

Haider MA, Sitartchouk I, Roberts TP, Fyles A, Hashmi AT, Milosevic M (2007) Correlations between dynamic contrast-enhanced magnetic resonance imaging-derived measures of tumor microvasculature and interstitial fluid pressure in patients with cervical cancer. *J Magn Reson Imaging* **25**: 153–159

Jain RK (2001) Normalizing tumor vasculature with anti-angiogenic therapy: a new paradigm for combination therapy. *Nat Med* **7**: 987–989

Jakowlew SB (2006) Transforming growth factor-beta in cancer and metastasis. *Cancer Metastasis Rev* **25**: 435–457

Kano MR, Bae Y, Iwata C, Morishita Y, Yashiro M, Oka M, Fujii T, Komuro A, Kiyono K, Kaminishi M, Hirakawa K, Ouchi Y, Nishiyama N, Kataoka K, Miyazono K (2007) Improvement of cancer-targeting therapy, using nanocarriers for intractable solid tumors by inhibition of TGF-beta signaling. *Proc Natl Acad Sci USA* **104**: 3460–3465

Kiessling F, Morgenstern B, Zhang C (2007) Contrast agents and applications to assess tumor angiogenesis *in vivo* by magnetic resonance imaging. *Curr Med Chem* **14**: 77–91

Koh DM, Padhani AR (2006) Diffusion-weighted MRI: a new functional clinical technique for tumour imaging. *Br J Radiol* **79:** 633-635

Li HY, Wang Y, Heap CR, King CH, Mundla SR, Voss M, Clawson DK, Yan L, Campbell RM, Anderson BD, Wagner JR, Britt K, Lu KX, McMillen WT, Yingling JM (2006) Dihydropyrrolopyrazole transforming growth factor-beta type I receptor kinase domain inhibitors: a novel benzimidazole series with selectivity versus transforming growth factor-beta type II receptor kinase and mixed lineage kinase-7. *J Med Chem* **49:** 2138-2142

Marzola P, Degrassi A, Calderan L, Farace P, Crescimanno C, Nicolato E, Giusti A, Pesenti E, Terron A, Sbarbati A, Abrams T, Murray L, Osculati F (2004) In vivo assessment of antiangiogenic activity of SU6668 in an experimental colon carcinoma model. *Clin Cancer Res* **10:** 739-750

Matsumura Y, Maeda H (1986) A new concept for macromolecular therapeutics in cancer chemotherapy: mechanism of tumoritropic accumulation of proteins and the antitumor agent smancs. *Cancer Res* **46:** 6387-6392

Morgan B, Thomas AL, Drevs J, Hennig J, Buchert M, Jivan A, Horsfield MA, Mross K, Ball HA, Lee L, Mietlowski W, Fuxuis S, Unger C, O'Byrne K, Henry A, Cherryman GR, Laurent D, Dugan M, Marme D, Steward WP (2003) Dynamic contrast-enhanced magnetic resonance imaging as a biomarker for the pharmacological response of PTK787/ZK 222584, an inhibitor of the vascular endothelial growth factor receptor tyrosine kinases, in patients with advanced colorectal cancer and liver metastases: results from two phase I studies. *J Clin Oncol* **21:** 3955-3964

Nakamura K, Taguchi E, Miura T, Yamamoto A, Takahashi K, Bichat F, Guilbaud N, Hasegawa K, Kubo K, Fujiwara Y, Suzuki R, Kubo K, Shibuya M, Isae T (2006) KRN951, a highly potent inhibitor of vascular endothelial growth factor receptor tyrosine kinases, has antitumor activities and affects functional vascular properties. *Cancer Res* **66:** 9134-9142

O'Connor JP, Jackson A, Parker GJ, Jayson GC (2007) DCE-MRI biomarkers in the clinical evaluation of antiangiogenic and vascular disrupting agents. *Br J Cancer* **96:** 189-195

Patterson DM, Padhani AR, Collins DJ (2008) Technology insight: water diffusion MRI–a potential new biomarker of response to cancer therapy. *Nat Clin Pract Oncol* **5:** 220-233

Tojo M, Hamashima Y, Hanyu A, Kajimoto T, Saitoh M, Miyazono K, Node M, Imamura T (2005) The ALK-5 inhibitor A-83-01 inhibits Smad signaling and epithelial-to-mesenchymal transition by transforming growth factor-beta. *Cancer Sci* **96:** 791-800

Tozer GM (2003) Measuring tumour vascular response to antivascular and antiangiogenic drugs. *Br J Radiol* **76:** S23-S35

Tsekos NV, Zhang F, Merkle H, Nagayama M, Iadecola C, Kim SG (1998) Quantitative measurements of cerebral blood flow in rats using the FAIR technique: correlation with previous iodoantipyrine autoradiographic studies. *Magn Reson Med* **39:** 564-573

Tsuchida K, Sunada Y, Noji S, Murakami T, Uezumi A, Nakatani M (2006) Inhibitors of the TGF-beta superfamily and their clinical applications. *Mini Rev Med Chem* **6:** 1255-1261

Turetschek K, Preda A, Novikov V, Brasch RC, Weinmann HJ, Wunderbaldinger P, Roberts TP (2004) Tumor microvascular changes in antiangiogenic treatment: assessment by magnetic resonance contrast media of different molecular weights. *J Magn Reson Imaging* **20:** 138-144

Van Zijl PC, Moonen CT, Faustino P, Pekar J, Kaplan O, Cohen JS (1991) Complete separation of intracellular and extracellular information in NMR spectra of perfused cells by diffusion-weighted spectroscopy. *Proc Natl Acad Sci USA* **88:** 3228-3232

＊研究論文＊

Intensity-Based Bayesian Framework for Image Reconstruction from Sparse Projection Data

Essam A. RASHED*, Hiroyuki KUDO*

Abstract

This paper presents a Bayesian framework for iterative image reconstruction from projection data measured over a limited number of views. The classical Nyquist sampling rule yields the minimum number of projection views required for accurate reconstruction. However, challenges exist in many medical and industrial imaging applications in which the projection data is undersampled. Classical analytical reconstruction methods such as FBP are not a good choice for use in such cases because the data undersampling in the angular range introduces aliasing and streak artifacts that degrade lesion detectability. In this paper, we propose a Bayesian framework for ML-EM-based iterative reconstruction methods that incorporates *a priori* knowledge obtained from expected intensity information. The proposed framework is based on the fact that, in tomographic imaging, it is often possible to expect a set of intensity values of the reconstructed object with relatively high accuracy. The image reconstruction cost function is modified to include the ℓ_1 norm distance to the *a priori* known information. The proposed method has the potential to regularize the solution to reduce artifacts without missing lesions that cannot be expected from the *a priori* information. Numerical studies showed a significant improvement in image quality and lesion detectability under the condition of highly undersampled projection data.

Key words: Tomography, Image reconstruction, Sparse projection data, Bayesian method, Compressed sensing

Med Imag Tech **27**(4): 243-251, 2009

1. Introduction

In Computed Tomography (CT), projection data of the target object is measured over a set of many view angles. The number of acquired projection views has a large influence to accuracy and stability of the image reconstruction. In many imaging applications, the projection data is available only over a limited number of views. The term *limited view projection data* (also called *sparse projection data*) refers to the case where the projection data is acquired over a small number of equally/unequally spaced angles less than the requirement by the Nyquist sampling rule [1]. It is well-known that image reconstruction from the sparse projection data is an underdetermined problem and the reconstructed image suffers from streak/aliasing artifacts that significantly degrade lesion detectability. **Fig. 1** shows two CT imaging configurations for the conventional full scan and sparse scan. We note that image reconstruction from the sparse projection data is an important problem in both medical and industrial imaging applications. In the following, we show examples for which the projection data becomes sparse. Electrocardiogram (ECG) gated cardiac CT is a novel imaging technique used in diagnosing coronary artery disease thanks to its remarkable ability to reduce cardiac motion artifacts [2]. The CT imaging is synchronized with the ECG signal representing the cardiac motion and the projection data is re-organized such that all views correspond to each ECG temporal

---

* Department of Computer Science, Graduate School of Systems and Information Engineering,University of Tsukuba
〔Tennoudai 1-1-1, Tsukuba 305-8573, Japan〕
e-mail: essam@imagelab.cs.tsukuba.ac.jp

receive: April 30, 2009
accept: July 30, 2009

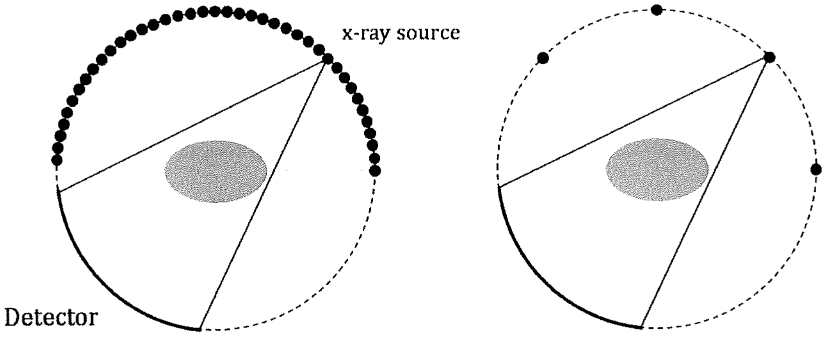

Fig. 1 Positions of x-ray source for CT data acquisition. The conventional full projection data (left) and the sparse projection data (right).

window. Even by using high-speed modern CT scanners, it is known that the re-organization of measured data still leads to a sparse projection data. Another important application of this paper is the nondestructive testing (NDT) in industry using CT techniques [3]. The NDT is used to examine internal cracks in various products and the sparse projection data occurs due to limitations in the scanner geometry, imaging setup and data acquisition time.

In the literature, different approaches have been investigated to reduce the streak/aliasing artifacts caused by the data undersampling. However, these approaches have not been used in commercial scanners yet. One direction to overcome this problem is to estimate missing projection data by iterative or non-iterative methods [4, 5]. Another direction is to incorporate *a priori* information for the scanned object into image reconstruction using Bayesian framework. The *a priori* information can be expressed in different forms, such as Gaussian smoothness prior [6] and Markov random field prior [7].

Recently, reconstruction of sparse signals/images is attracting attention of many research groups. Here, the term *sparse image* means that the image to be reconstructed contains a small number of non-zero pixels. The recently emerged theories of compressed sensing [8] demonstrate that it is possible to reconstruct accurate images using projection data measured over a small number of views fewer than the traditional requirement [9, 10]. The main idea is to include a distance function consisting of ℓ_1/ℓ_0 norm of the reconstructed image into the cost function for image reconstruction. Our group also applied this concept to blood vessel reconstruction [11], Anatomical-MAP PET/SPECT reconstruction [12] and image reconstruction from truncated projection data [13]. Reconstruction methods based on the compressed sensing have been also developed for respiratory-gated cone-beam CT [14] and MRI imaging [15].

In this paper, we propose a new Bayesian framework to develop iterative image reconstruction methods from the sparse projection data. In the compressed sensing framework, the image sparseness is enforced by transforming the image into some domain (e.g. gradient or wavelet) such that the majority of coefficients are approximately zeros. However, the sparsity assumption of object is not necessary in the proposed framework, as most applications in CT deal with non-sparse objects. In the following, we explain the main idea of the proposed framework. Assuming that $\vec{x}$ denotes the image vector, we represent the reconstructed image as a sum of two components; the *reference image* ($\vec{x}^R$) which includes all regions expected from the *a priori* known information (such as bones, soft tissues,..., etc) and the *target image* ($\vec{x}^T$) which includes unknown regions (such as lesions) that cannot be expected from the *a priori* information, as shown in **Fig. 2**. Medical imaging dedicated for diagnosis as well as NDT applications, in many cases, aims at discovering the existence of $\vec{x}^T$ in the scanned object and/or detecting a temporal change or an individual difference in the image. By using this image model, we consider the following two imaging scenarios. In the first scenario, we assume that $\vec{x}^R$ is *a priori* known with high accuracy. This *a priori* information can be obtained, for example, by using the image reconstructed from all measured projection data in ECG gated cardiac CT. The reference image in this case is known to be blurred due to the motion artifacts but is still valid to be used as $\vec{x}^R$. In the second scenario, we assume that both $\vec{x}^T$ and $\vec{x}^R$ are *a priori* unknown but a set of intensity values

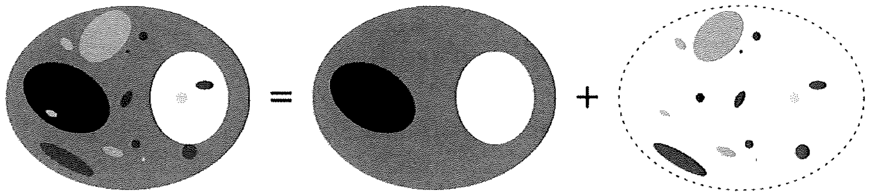

Fig. 2 The image model used in the proposed Bayesian framework. Reconstructed image $\vec{x}$ (left), reference image $\vec{x}^R$ (middle) and target image $\vec{x}^T$ (right).

$\vec{m} = (m_1, \dots, m_H)$ used to represent $\vec{x}^R$ are known in prior to image reconstruction. The term *intensity value* refers to the value of x-ray attenuation coefficient contained in the reference image $\vec{x}^R$. Each component of $\vec{m}$ corresponds to an intensity value of a single region (organ) in $\vec{x}^R$. For example, the intensity values for air, water, lung, and sternum for x-ray radiation of 70kev are known to be almost 0.0 (cm^{-1}), 1.0 (cm^{-1}), 0.26 (cm^{-1}), and 1.25 (cm^{-1}), respectively. Compared to the first scenario, the second scenario is not so difficult to be used in many CT applications. For example, in chest imaging, the intensity values of organs can be accurately expected by using a previous scan of the same patient, an image averaged for different patients or commonly known intensity values. Moreover, $\vec{m}$ can be estimated from the histogram of initial image reconstructed from the sparse projection data. We note that our group has already proposed a theoretically similar framework to the one proposed here for the first scenario. That framework was used to reconstruct PET/SPECT images with superior noise/contrast properties using template images estimated from CT/MRI [12]. Also, a related work to the reconstruction method proposed for the first scenario was recently published [14]. To the best of our knowledge, the reconstruction method proposed for the second scenario is an original contribution. This paper is organized as follows. In section 2, the proposed Bayesian framework and the associated iterative reconstruction methods are explained. In section 3, numerical studies performed to evaluate the proposed framework are shown. In section 4, conclusion and future work are described.

2. Methodology

1) Problem definition

The aim of CT imaging is to reconstruct an object from measured projection data. When iterative techniques are used for image reconstruction, this problem can be formulated as solving the linear equation $A\vec{x} = \vec{y}$ where $\vec{x} = (x_1, \dots, x_n)$ is the discrete representation of object, $A = \{a_{ij}\}$ is the $m \times n$ system matrix and $\vec{y} = (y_1, \dots, y_m)$ is the measured projection data. When the dimension of $\vec{y}$ is smaller than the dimension of $\vec{x}$ (i.e. $m < n$), this problem becomes underdetermined and reconstructing an accurate image becomes challenging. To overcome this problem, the so-called Bayesian method takes *a priori* information on the scanned object into account. The proposed Bayesian framework is based on the image model that the reconstructed image $\vec{x}$ can be represented as $\vec{x} = \vec{x}^R + \vec{x}^T$ as stated in section 1. Given $\vec{y}$ measured over a small number of views, the proposed reconstruction method is based on minimizing the following cost function.

$$f_\beta(\vec{x}) = L(\vec{x}) + \beta D(\vec{x}) \tag{1}$$

$$L(\vec{x}) = \sum_{i=1}^{m}\left[\sum_{j=1}^{n} a_{ij}x_j - y_i \log\left(\sum_{j=1}^{n} a_{ij}x_j\right)\right] \tag{2}$$

The formulation of **Eq. (1)** is well-known as maximum *a posteriori* (MAP) reconstruction, where $L(\vec{x})$ is the negative log-likelihood function, $D(\vec{x})$ is the distance function between the reconstructed image $\vec{x}$ and the available *a priori* information (described below) and β is the hyperparameter to control the strength of prior information. The distance function $D(.)$ can be formulated in various forms dependent on image properties and the nature of available *a priori* information. In this paper, we consider image reconstruction corresponding to the two scenarios described in section 1. In the first scenario (i.e. the *a priori* information takes the form of reference image $\vec{x}^R$), we propose the distance function as

$$D(\vec{x}) \equiv D_R(\vec{x}, \vec{x}^R) = \sum_{j=1}^{n} d(x_j, x_j^R). \tag{3}$$

In the second scenario, (i.e. the *a priori* information is a set of intensity values $\vec{m}$), we propose the distance function as

$$D(\vec{x}) \equiv D_I(\vec{x}, \vec{m}) = \sum_{j=1}^{n} \min_h [\omega_h d(x_j, m_h)] \tag{4}$$

The distance function in **Eq. (3)** simply measures the sum of pixel-by-pixel distance between $\vec{x}$ and $\vec{x}^R$. On the other hand, the distance function in **Eq. (4)** is defined as the sum of pixel-by-pixel minimum distance measured between each image pixel x_j and the set of *a priori* known intensity values m_h $(h = 1, \ldots, H)$. The parameters $\omega_1, \ldots, \omega_H$ represent weights corresponding to the components of $\vec{m}$. For example, the weights $\omega_1, \ldots, \omega_H$ can be determined from the estimated intensity histogram of reference image $\vec{x}^R$ (i.e. ω_h should be large if many pixels in $\vec{x}^R$ have the intensity m_h). The single variable distance function $d(.,.)$ should be carefully selected because it has a large influence on the reconstructed image [12]. The conventional selection is the least square distance (i.e. ℓ_2 norm of $\vec{x} - \vec{x}^R$), however, we have found that a good choice that guarantees the convergence of associated iterative methods and, at the same time, achieves significantly better image quality is the ℓ_1 norm defined by

$$d(a, b) = |a - b|. \tag{5}$$

In the following section, we discuss some property of the ℓ_1 norm that clarifies why ℓ_1 norm is the proper distance to be used in **Eqs. (3)** and **(4)**.

2) Power of ℓ_1 norm distance

We explain why the ℓ_1 norm behaves powerfully compared to the conventional ℓ_2 norm in finding a solution of the problem discussed above [11, 12]. We first note that, in the proposed image model (**Fig. 2**), $\vec{x}$ is relatively close to $\vec{x}^R$ as lesions (i.e. unexpected abnormal regions) usually arise in a small region. Therefore, the difference between $\vec{x}$ and $\vec{x}^R$ corresponding to $\vec{x}^T$ becomes a sparse image. Let us consider the simple case of a two-components image $\vec{x} = (x_1, x_2)$ and a single-component projection data $\vec{y} = (y_1)$. **Fig. 3** illustrates equi-contour lines corresponding to the ℓ_p norm with $p = 1$ and $p = 2$. The dashed line $\mathcal{L}$ represents the linear equation $a_{11}x_1 + a_{12}x_2 = y_1$. In this case, the intersection point between $\mathcal{L}$ and x_1 (or x_2) axis (centered at the reference image $\vec{x}^R$) is the sparse solution which we would like to reconstruct. From the equi-contour lines shown in **Fig. 3**, it is clear that the ℓ_1 norm distance gives a larger cost to the points far from the coordinate axes (i.e. non-sparse solutions) compared to the ℓ_2 norm. Consequently, we expect that the ℓ_1 norm distance has a stronger power in finding sparse solutions on or near the coordinate axes. This fact has been demonstrated in a few examples by our previous work [11, 12]. In higher-dimension problems, the difference between the ℓ_1 and ℓ_2 norms can be significant. This clarifies that, when the solution is sparse, the use of ℓ_1 norm is the method of choice. Though the ℓ_p norm with $0 < p < 1$ has a stronger power from this point of view, we preferred to use the ℓ_1 norm because the convergent iterative method is known for the ℓ_1 norm [16].

3) Iterative reconstruction methods

The main obstacle in using the ℓ_1 norm is the lack of convexity and differentiability of the cost function $f_\beta(\vec{x})$. Overcoming this drawback was made possible by using the so-called majorization-minimization strategy [16]. The derivation of iterative reconstruction methods to minimize $f_\beta(\vec{x})$ is based on majorizing the non-separable part of $f_\beta(\vec{x})$ by a separable quadratic function around the current iterate $\vec{x} = \vec{x}^{(k)}$ (k is the iteration number) and then minimizing the resulting cost function at each iteration. The detailed derivation using this technique can be found in [12] (we will not repeat the derivation here). The final form of the iterative methods is expressed as repeating the following two-substep procedure. The first substep is the normal image update of standard maximum likelihood expectation-maximization (ML-EM) algorithm, and the second substep is the thresholding operation which rule is determined by the *a priori* information. In the following, we outline the final form of two iterative methods associated with the two different imaging scenarios described in section 1. The main difference between the two methods

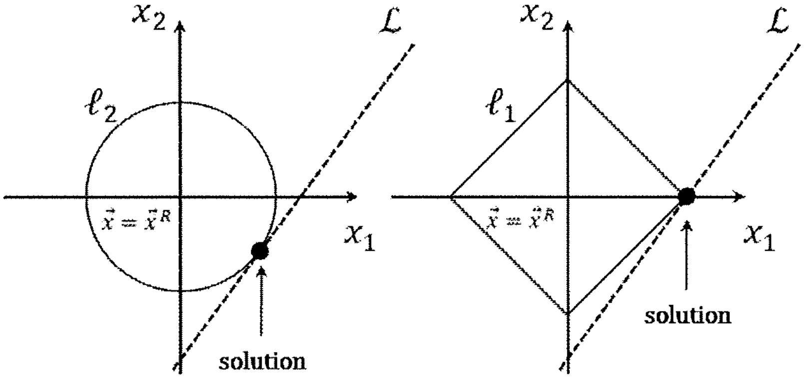

Fig. 3 Equi-contour lines of the ℓ_p norm distance with $p = 2$ (left) and $p = 1$ (right). $\mathcal{L}$ is the straight line representing the linear equation to be solved and the solid point represents the solution obtained by minimizing the ℓ_p norm distance.

is the nature of *a priori* information and the way to incorporate it into the cost function. The first method, R-MAP (Reference-MAP) is used in the case where the reference image $\vec{x}^R$ is available. On the other hand, the second method, I-MAP (Intensity-MAP) is used in the case where the *a priori* information is limited to only a set of intensity values $\vec{m} = (m_1, \dots, m_H)$ arranged in ascending order (i.e. $m_1 < m_2 < \cdots < m_H$). The R-MAP and I-MAP methods are summarized as follows.

R-MAP reconstruction method

[STEP 1] (Preprocessing) Prepare the reference image $\vec{x}^R$.

[STEP 2] (Initialization) Set the initial image as $\vec{x}^{(0)} = \vec{x}^R$. Set the iteration number as $k \leftarrow 0$.

[STEP 3-1] (EM-update) Compute the image vector $\vec{p} = (p_1, p_2, \dots, p_n)$ by

$$p_j = \frac{x_j^{(k)}}{\sum_{i=1}^{m} a_{ij}} \sum_{i=1}^{m} \frac{a_{ij} y_i}{\sum_{j'=1}^{n} a_{ij'} x_{j'}^{(k)}} \ . \tag{6}$$

[STEP 3-2] (Intensity thresholding) Compute the image vector $\vec{q} = (q_1, q_2, \dots, q_n)$ by

$$q_j = \begin{cases} p_j - \delta_j & p_j > x_j^R + \delta_j \\ p_j + \delta_j & p_j < x_j^R - \delta_j \\ x_j^R & elsewhere \end{cases} , \quad \delta_j = \frac{\beta x_j}{\sum_i a_{ij}} \ . \tag{7}$$

[STEP 3-3] (Image update) Compute $\vec{x}^{(k+1)} = (x_1^{(k+1)}, x_2^{(k+1)}, \dots, x_n^{(k+1)})$ by $x_j^{(k+1)} = \max\,(q_j, \epsilon)$, where $\epsilon > 0$ is a small number to ensure the positivity of pixel value (this technique is sometimes used in ML-EM-based iterative algorithms to avoid dividing by zero in **Eq. (6)**).

[STEP 4] (Convergence check) Increment the iteration number as $k \leftarrow k + 1$ and go to **[STEP 3-1]** until reaching to a stopping criteria.

I-MAP reconstruction method

[STEP 1] (Preprocessing) Prepare the set of *a priori* known intensity values $\vec{m}$.

[STEP 2] (Initialization) Set the initial image as $\vec{x}^{(0)} = \varepsilon$ where $\varepsilon > 0$ is a small positive number. Set the iteration number as $k \leftarrow 0$.

[STEP 3-1] (EM-update) Compute the image vector $\vec{p} = (p_1, p_2, \dots, p_n)$ by **Eq. (6)**.

[STEP 3-2] (Intensity thresholding) Compute the image vector $\vec{q} = (q_1, q_2, \dots, q_n)$ by

$$q_j = \begin{cases} p_j + \delta_{j,1} & p_j < M_{j,1}^- \\ m_1 & M_{j,1}^- \le p_j \le \min\left(M_{j,1}^+, s_1\right) \\ p_j - \delta_{j,1} & M_{j,1}^+ < p_j \le s_1 \\ \vdots & \\ p_j + \delta_{j,h} & s_{h-1} < p_j < M_{j,h}^- \\ m_h & \max\left(M_{j,h}^-, s_{h-1}\right) \le p_j \le \min\left(M_{j,h}^+, s_h\right), \quad h = 2,3,\ldots,H-1 \\ p_j - \delta_{j,h} & M_{j,h}^+ < p_j \le s_h \\ \vdots & \\ p_j + \delta_{j,H} & s_{H-1} < p_j < M_{j,H}^- \\ m_H & \max\left(M_{j,H}^-, s_{H-1}\right) \le p_j \le M_{j,H}^+ \\ p_j - \delta_{j,H} & p_j > M_{j,H}^+ \end{cases} \tag{8}$$

where $\delta_{j,h} = \left(\beta x_j^{(k)} \omega_h\right) / \left(\sum_i a_{ij}\right), s_h = \left(\omega_h m_h + \omega_{h+1} m_{h+1}\right) / \left(\omega_h + \omega_{h+1}\right), M_{j,h}^- = m_h - \delta_{j,h}$ and $M_{j,h}^+ = m_h + \delta_{j,h}$.

[STEP 3-3] (Image update) Compute $\vec{x}^{(k+1)} = \left(x_1^{(k+1)}, x_2^{(k+1)}, \ldots, x_n^{(k+1)}\right)$ by $x_j^{(k+1)} = \max\ (q_j, \epsilon)$.

[STEP 4] (Convergence check) Increment the iteration number as $k \leftarrow k+1$ and go to **[STEP 3-1]** until reaching to a stopping criteria.

The thresholding function in **Eq. (7)** for the R-MAP method has the form of well-known soft-thresholding used in the wavelet denoising. In practical implementation, the soft-thresholding trims the image pixel value p_j in **[STEP 3-2]** toward the value of x_j^R when they are relatively close, otherwise, p_j is shifted "softly" toward x_j^R. On the other hand, the thresholding function in **Eq. (8)** for the I-MAP method can be expressed as a combination of multiple successive soft-thresholding functions. The meaning of this thresholding is as follows. If the pixel value p_j is close to any component m_h of the intensity vector $\vec{m}$ (i.e. located inside the thresholding window controlled by the parameter ω_h), p_j is trimmed to m_h. Otherwise, p_j is shifted "softly" toward the closest value among $m_1, m_2, \ldots, m_H$. The thresholding functions in both methods are designed to find the correct pixel value using the *a priori* information when the projection data is sparse. As shown later, the proposed framework significantly reduces the streak/aliasing artifacts.

3. Experimental results

1) Numerical phantom

In this simulation, we implemented ordered-subsets versions of the proposed methods (R-MAP and I-MAP) and the conventional OS-EM method. The phantom shown in **Fig. 2** was used and noise free projection data was used for image reconstruction. The image size was 512×512 (pixels) and the projection data was computed by parallel-beam geometry with 512 (radial bins) and 8/16 views (over 180°). In this phantom, the pixel intensity value inside each region is uniform. For the R-MAP method, we assumed that the accurate reference image $\vec{x}^R$ is *a priori* known with no registration errors (ideal setup). For the I-MAP method, the intensity values representing the *a priori* information were $\vec{m}$ = (0.0, 0.2, 1.0, 2.0), where the value of zero corresponds to the region outside the object (air) and the other values correspond to the three regions in the reference image $\vec{x}^R$. All the iterative methods were implemented with 300 iterations and 4 subsets. The main aim of this simulation was to evaluate detectability of unexpected regions (lesions) $\vec{x}^T$ in the reconstructed image when the projection data is sparse. The reconstructed images are shown in **Fig. 4**. In the conventional OS-EM images, the severe streak/aliasing artifacts are present and the contrast of reconstructed lesions $\vec{x}^T$ is low, which reduces possibility of detecting the lesions. However, a significant improvement in the lesion detectability was achieved in both the R-MAP and I-MAP methods. By using only 16 projection views, most of lesions with different size, contrast, and topology were recognized. As described in [12], the R-MAP method, which uses the reference image $\vec{x}^R$, is sensitive to registration errors between $\vec{x}$ and $\vec{x}^R$. However, this is not the case for the I-MAP method. Moreover, as explained above, the required *a priori* information for the I-MAP method is significantly smaller than that for the R-MAP method.

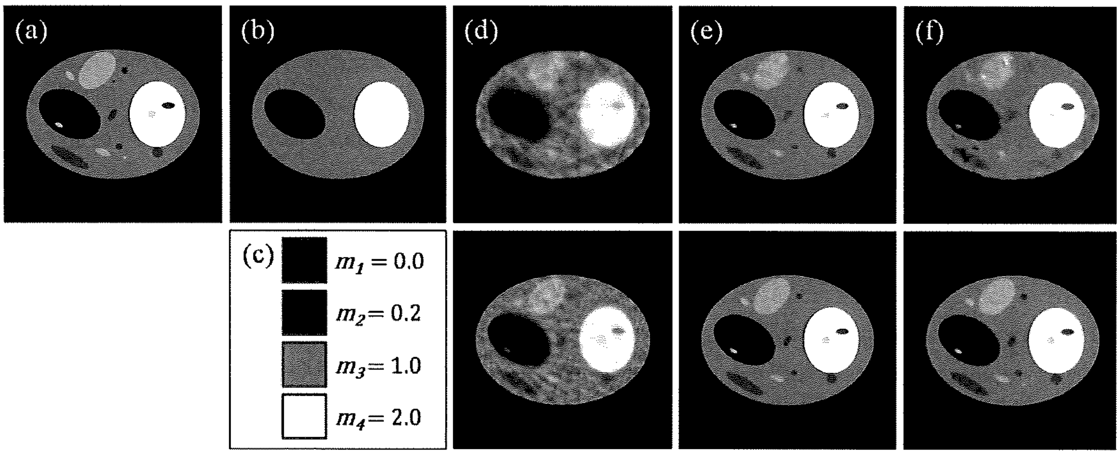

Fig. 4 (a) Numerical phantom, (b) the reference image $\vec{x}^R$ for the R-MAP method and (c) intensity values $\vec{m}$ for the I-MAP method. Reconstructed images using (d) the conventional OS-EM, (e) R-MAP and (f) I-MAP methods (8 views in top row and 16 views in bottom row). The gray scale is [0.0, 2.0].

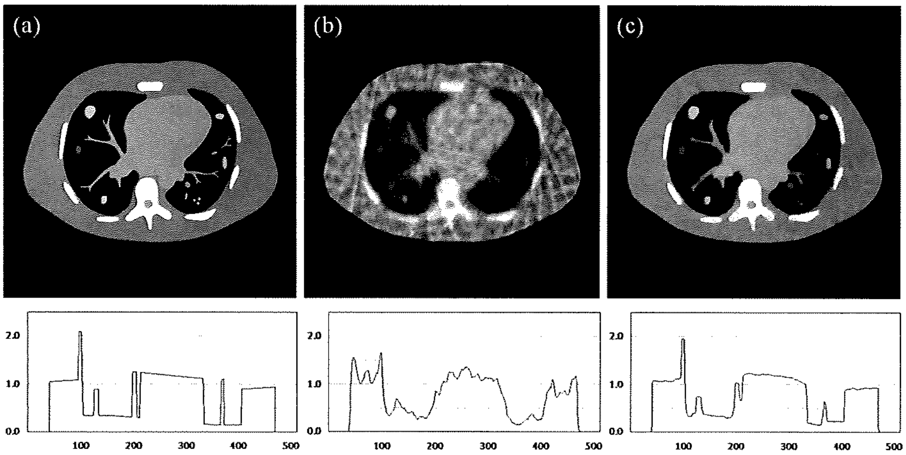

Fig. 5 (a) Chest phantom. Images (top) and central horizontal profiles (bottom) reconstructed from 16 projection views using (b) OS-EM and (c) I-MAP methods. The gray scale is [0.0, 2.0].

2) Realistic chest phantom

In clinical CT applications, the attenuation coefficient within the same organ is not absolutely uniform in general. In this study, a realistic chest phantom was used to evaluate the I-MAP method. The phantom represents a slice of human thorax and the intensity value within each region (organ) is non-uniform as shown by the profile plot in **Fig. 5(a)**. A 2D Gaussian fluctuation function was used to generate this phantom from the original segmented chest image. The chest phantom contains lung lesions with different topology, size and contrast together with the blood-vessel structures as shown in **Fig. 5(a)**. To handle the effect of intensity variation within the same region, the distance function in **Eq. (5)** was modified as

$$d(a,b) \equiv \tilde{d}(a,b,\Delta) = \begin{cases} a-b-\Delta & (a-b>\Delta) \\ b-a-\Delta & (a-b<-\Delta) \\ 0 & (otherwise) \end{cases}, \tag{9}$$

where Δ is the parameter empirically determined by the degree of intensity fluctuation within the same region. The derivation of the corresponding thresholding function in this case is direct and is omitted. The *a priori* information for the I-MAP method $\vec{m}$ = (0.0, 0.26, 1.0, 1.2, 2.0) represents values of attenuation coefficients corresponding to air, lungs, soft tissues, heart and bones. $\vec{m}$ was computed as average values of each region. In this study, the image model in **Fig. 2** was used under the assumption that the reference image $\vec{x}^R$ contains normal thorax structures (i.e. lungs, soft-tissue, heart and bones), but does not contain the other unexpected structures. On the other hand, the target image $\vec{x}^T$ contains the unexpected structures such as lesions (with different topology, size and contrast) and blood-vessels located inside the lungs. Therefore, the purpose of image reconstruction here was to improve detectability (contrast and spatial resolution) of the lesions and blood-vessels $\vec{x}^T$ in the reconstructed image when the projection data is sparse. Of course, in the I-MAP method, only the intensity values constructing the normal structures were used instead of the reference image $\vec{x}^R$ itself. The projection data was computed over 16 views and other simulation setups were similar to those in the previous study. The reconstructed images shown in **Fig. 5** demonstrate that the conventional OS-EM reconstruction suffers from severe streak/aliasing artifacts and low-contrast in the lung lesions so that lesion detectability is poor. On the other hand, by using the I-MAP, most of lesions can be recognized correctly by reducing the image artifacts and recover the contrast of lesions and blood vessels. The proposed I-MAP method still works well even if intensity value within the same region is slightly non-uniform.

4. Conclusions

We proposed a Bayesian framework to develop iterative image reconstruction methods in CT when the projection data is sparse. The proposed framework is appropriate to reduce streak/aliasing artifacts by using *a priori* information on intensity values of scanned object. The main contribution of this paper was to reduce the required *a priori* information for image improvement to only a set of intensity values, whereas the previous similar methods assumed that the reference image is accurately known. The cost function for image reconstruction was designed by adding a distance function based on the ℓ_1 norm, which compares each pixel value of reconstructed image to the *a priori* known intensity values. We think that the *a priori* information on the intensity values is relatively easy to obtain in many clinical CT imaging situations and, therefore, the proposed framework sounds practical. The reconstructed images in the numerical studies show that the proposed framework can significantly reduce image artifacts and preserve image details unexpected from the *a priori* knowledge even if the intensity values within the same region are non-uniform. Applying the proposed framework to real patient data is currently under investigation. Future work may include investigating possible approaches to obtain the *a priori* information in various imaging situations and extending the proposed method to the limited angle and truncation problems.

Finally, we remark that the proposed Bayesian framework is general such that it has a potential to be used in the other limited-data problems. However, we expect that its validity and power strongly depend on the type of image artifacts to be eliminated by the use of *a priori* knowledge. Since such experimental evaluation must be done dependent on the type of limited-data, as a first step, this paper limited the focus-of-attention to the case of "sparse projection data", just due to the fact that it is simplest among all the limited-data problems. We will publish experimental results for the other limited-data problems in separate publications [13].

References

[1] Natterer F: The Mathematics of Computerized Tomography. Wiley: New York, 1986

[2] Desjardins B, Kazerooni EA: ECG-gated cardiac CT. Am J Roentgenol **182**: 993-1010, 2004

[3] Tam KC, Eberhard JW, Mitchell KW: Incomplete-data CT image reconstructions in industrial applications. IEEE Trans Nucl Sci **37**: 1490-1499, 1990

[4] Nassi M, Brody WR, Medoff BP et al: Iterative reconstruction-reprojection: An algorithm for limited data cardiac-computed tomography. IEEE Trans Biomed Eng **29**: 333-341, 1982

[5] Galigekere RR, Wiesent K, Holdsworth DW: Techniques to alleviate the effects of view aliasing artifacts in computed tomography. Med Phys **26**: 896-904, 1999

[6] Hanson KM, Wecksung GW: Bayesian approach to limited-angle reconstruction in computed tomography. J Opt Soc Am **73**: 1501-1509, 1983

[7] Sauer K, Sachs J Jr, Klifa C: Bayesian estimation of 3-D objects from few radiographs. IEEE Trans Nucl Sci **41**: 1780-1790, 1994

[8] Donoho DL: Compressed sensing. IEEE Trans Inf Theory **52**: 1289-1306, 2006

[9] Candès EJ, Romberg J, Tao T: Robust uncertainty principles: Exact signal reconstruction from highly incomplete frequency information. IEEE Trans Inf Theory **52**: 489-509, 2006

[10] Chartrand R: Exact reconstruction of sparse signals via nonconvex minimization. IEEE Signal Process Lett **14**: 707-710, 2007

[11] Li M, Yang H, Kudo H: An accurate iterative reconstruction algorithm for sparse objects: application to 3D blood-vessel reconstruction from limited number of projections. Phys Med Biol **47**: 2599-2609, 2002

〔12〕 Mameuda Y, Kudo H: New anatomical-prior-based image reconstruction method for PET/SPECT. Conference Record of 2007 IEEE Medical Imaging Conference: Paper No. M23-2, 2007

〔13〕 Rashed EA, Kudo H: Region-of-interest reconstruction from truncated projection data under blind object support. Conference Record of 2008 IEEE Medical Imaging Conference: Paper No. M03-7, 2008

〔14〕 Leng S, Tang J, Zambelli J et al: High temporal resolution and streak-free four-dimensional cone-beam computed tomography. Phys Med Biol **53**: 5653-5673, 2008

〔15〕 Trzasko J, Manduca A: Highly undersampled magnetic resonance image reconstruction via homotopic ℓ_0-minimization. IEEE Trans Med Imag **28**: 106-121, 2009

〔16〕 Daubechies I, Defrise M, De Mol C: An iterative thresholding algorithm for linear inverse problems with a sparsity constraint. Comm Pure Appl Math **57**: 1413-1457, 2004

疎な投影データからの画像再構成のための濃度情報に基づくベイズ推定の枠組み

イサム A. ラシド*　工藤博幸*

*筑波大学大学院システム情報工学研究科コンピュータサイエンス専攻

要旨：本論文では，少数方向投影データからの逐次近似画像再構成のためのベイズ推定の新しい枠組みを提案する．正確な画像再構成に必要な投影データの方向数はナイキスト間隔により与えられるが，医療用や工業計測用のCTでは少数方向の投影データしか計測できない状況が起きる．このような場合，FBP法などの解析的画像再構成法では画像にストリーク状のエリアシングアーティファクトが生じ，病変検出能が低下する．本論文では，画像の濃度値に関する事前情報をML-EM法に基づく逐次近似法に組み入れて画質を改善するベイズ推定の枠組みを提案する．提案手法は，多くのCTイメージングの状況において，画像にどのような濃度値の物体が含まれているかは比較的高い精度で予想できる事実に基づいている．提案手法では，画像再構成の評価関数に事前情報と再構成画像のL1ノルム距離を組み入れ，これにより事前情報から外れた病変を保存したままストリークアーティファクトを低減できる．数値ファントムと実CT画像から作成したファントムを用いたシミュレーション実験により，提案手法により少数方向の投影データから画質と病変検出能を大幅に改善した画像が得られることを示す．

キーワード：トモグラフィ，画像再構成，疎な投影データ，ベイズ推定，圧縮センシング
Med Imag Tech **27**(4): 243-251, 2009

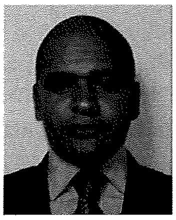

Essam A. Rashed（イサム　ラシド）

Received his B.Sc. in scientific computing (with honors) and M.Sc. in computer science in 1998 and 2002 from Suez Canal Univ., Egypt, respectively. Now, he is with the doctoral program in systems and information engineering, Univ. of Tsukuba. His research interests include computed tomography and medical image processing. He is a winner of the Egyptian Government national scholarship (2006) and JAMIT best presentation award (2008). He is a member of IEEE NPSS and JAMIT.

工藤博幸（くどう　ひろゆき）

1985年東北大・工・通信卒．1990年同大大学院博士課程了．現在，筑波大・システム情報・教授．1990年電子情報通信学会論文賞，1991年・2001年・2006年・2008年日本医用画像工学会論文賞，2006年・2008年国際雑誌『Inverse Problems』High Lights，2008年国際雑誌『Physics in Medicine and Biology』High Lights受賞．工博．CTとPETを中心とした医用イメージング，画像処理の研究に従事．IEEE，電子情報通信学会，各会員．2008年にCTの未解決問題であるInterior Problemの安定な厳密解法を発見し，これに関する2つの論文が国際雑誌『Physics in Medicine and Biology』と『Inverse Problems』の2008 High Lightsを受賞した．

* * *

＊研究論文＊

Iterative Region-of-Interest Reconstruction From Truncated CT Projection Data Under Blind Object Support

Essam A. RASHED*[1], Hiroyuki KUDO*[1], Frédéric NOO*[2]

Abstract

We have investigated image reconstruction from truncated projection data in computed tomography. Region-of-interest (ROI) imaging techniques, which are practically implemented by limiting X-ray exposure to the target region of the object, provide so-called truncated projection data. This limitation in the projection data converts the image reconstruction problem to an undetermined problem in which extra effort is needed to achieve accurate ROI reconstruction. Recently developed theories based on differentiated backprojection (DBP) suggest the possibility of achieving accurate ROI imaging in some clinical imaging scenarios. An essential requirement for achieving exact ROI reconstruction is prior knowledge of the object support (OS). However, the exact OS is not always available in many imaging applications. In this paper, first, we investigate how the image artifacts depend on the accuracy of the *a priori* known OS, and second, we propose an EM-based iterative reconstruction algorithm to reduce the ROI artifacts when the OS is unknown. The image reconstruction cost function is modified to include a thresholding function in the form of ℓ_0 norm, and thanks to this modification, the OS is automatically detected by the thresholding function and the ROI artifacts are reduced. The experimental results, including numerical simulations and real data with different ROI and object configurations, indicate that a significant reduction in ROI artifacts can be achieved by using the proposed algorithm.

Key words: Tomography, Image reconstruction, ROI imaging, Truncated projection data, Object support
Med Imag Tech **27**(5): 321-331, 2009

1. Introduction

Computed Tomography (CT) has become the most popular medical imaging modality to diagnose various diseases. The widespread use of CT increased the radiation dose in the population as CT involves much higher dose over the traditional plain-film radiography [1]. The interest was recently focused on developing reconstruction algorithms from low dose CT projection data to reduce the radiation dose. The dose reduction is challenging as the decreasing of the x-ray beam intensity increases the statistical noise in the reconstructed images. One possible approach to achieve the dose reduction is the Region-of-Interest (ROI) CT imaging by focusing the radiation only to the organ of interest, which reduces unnecessary radiation to the remaining portion of the patient. This imaging setup directly leads to data truncation problem in which left and/or right portions of the projection data are missing for all the view angles. **Fig. 1** illustrates CT imaging setups for the full scan and the ROI scan. The topic of ROI imaging has been studied for a long time (e.g. [2 ~ 5]) and, based on the concept of analytical reconstruction, it had been believed that ROI reconstruction, even for a small ROI, requires all projection rays passing through the whole object and any truncation leads to losing the solution exactness. However, the recently developed theories based on

---

*1 Department of Computer Science, Graduate School of Systems and Information Engineering, University of Tsukuba
〔Tennoudai 1-1-1, Tsukuba 305-8573, Japan〕
*2 Department of Radiology, University of Utah, UT, USA
e-mail: essam@imagelab.cs.tsukuba.ac.jp
receive: April 20, 2009
accept: october 8, 2009

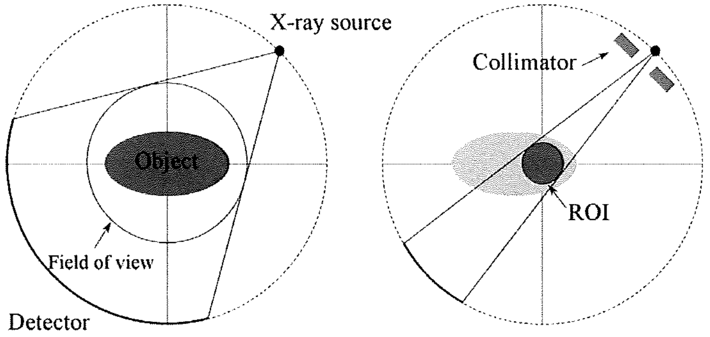

Fig. 1 CT imaging configurations for whole object imaging (left) and ROI imaging (right).

the concept of Differentiated Backprojection (DBP) [6] and Backprojection-Filtration (BPF) [7] succeeded in reducing the required set of projection rays for theoretically exact and stable ROI reconstruction. It became clear that the position of the ROI is an important factor to determine the possibility of accurate ROI reconstruction. Defrise et al. [8] provided a sufficient condition for accurate ROI reconstruction with truncated projection data. The exact reconstruction requires that the ROI contains a small limited region inside [9, 10] or outside the object with known intensity values. Practically, the availability of accurate prior information inside the object is difficult, however selecting this region as a portion of the background is more feasible as the attenuation value of air is known to be almost zero. Enforcing this *a priori* information of the background region is usually done using the Object Support (OS) constraint during image reconstruction. The OS is the region where the object is certainly inside. In real applications, however, the *a priori* knowledge of the OS is not always available or requires extra efforts to be estimated accurately. Alternatively, OS is selected a slightly larger than the true object to ensure that the object is located completely inside. Through numerical studies, it is known that the lack of exact OS produces DC-shift and low-frequency artifacts in the reconstructed images [11, 12].

The aim of this paper is two-fold. The first aim is to evaluate the relation between the accuracy of prior knowledge of OS constraint and the quality of image reconstructed from truncated projection data. The second aim is to propose an iterative ROI reconstruction algorithm from truncated projection data when the OS is unknown or technically unavailable. Throughout this paper, we consider the truncated projection data such that only the projection rays passing through the ROI are measured. These settings are suitable to achieve a reduction in the radiation exposure outside the ROI. In the proposed algorithm, the cost function is modified to include a thresholding function in the form of ℓ_0 norm distance. The OS is then automatically estimated by the thresholding function and iteratively converges towards the exact one. In section 2, we explain necessary basic concepts and the proposed iterative reconstruction algorithm. In section 3, we present numerical results of simulation studies and real data. In section 4, we conclude the paper.

2. Methodology

1) Object support constraint

We assume that the projection data is truncated such that it includes only the projection rays corresponding to all lines passing through a limited ROI $\mathbf{\Omega}$. We represent the OS (the *a priori* known region where the object is certainly inside) by μ. Then, the exact reconstruction of $\mathbf{\Omega}$ is possible if there exists a set of pixels x_j such that $x_j \in \mathbf{\Omega}$ and $x_j \notin \mu$ [8]. In other words, ROI should be defined such that it includes a limited region outside the OS where the intensity value is *a priori* known to be zero. Two different imaging configurations are shown in **Fig. 2** that illustrates Defrise's condition. In the setup of (a), the exact reconstruction is possible as the ROI is selected such that it contains a small region outside the OS μ (hatched area), while the exact reconstruction is theoretically not possible in the setup of (b) as it corresponds to the so-called *interior problem* [13]. The challenging of this theory is that, when the accuracy of OS is worse, the observed ROI should be selected to cover a larger region of the scanned

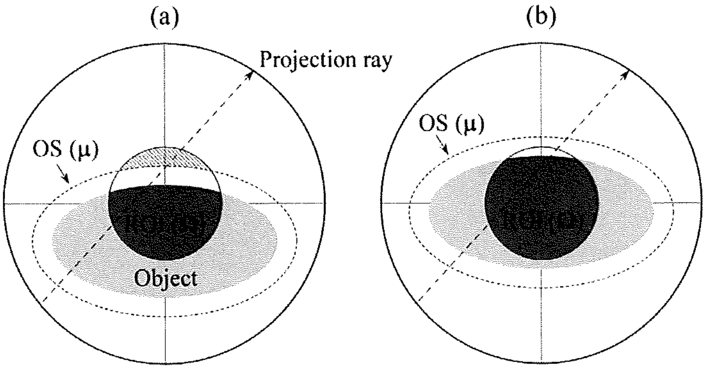

Fig. 2 Two different ROI imaging configurations, (a) ROI contains a region (shaded) outside the OS (Defrise's condition is satisfied and the solution exactness is assured) and (b) ROI is contained completely inside the OS (interior problem and the solution is not unique).

object and a larger area outside the object. A typical clinical application that demonstrates these imaging configurations is the cardiac ROI imaging. To obtain a theoretically accurate reconstruction, the ROI should be selected carefully such that it includes a region where the intensity value is *a priori* known to be zero. Considering the fact that it is difficult to determine the exact contours for different patients (exact OS) in prior to imaging, the ROI should be selected large enough to include the target object (heart) and the region outside the OS similarly to the setup of **Fig. 2**(a). The aim of this work is to estimate the exact OS during image reconstruction. This will allow us to reduce the size of ROI leading to dose reduction and other benefits. Finally, we remark that analytical solution have not been found yet for this truncation problem so that using iterative algorithms is an only way to perform image reconstruction in this problem 〔8~10〕.

2) Iterative algorithms with zero-pixels identification

To estimate the OS, for example, iterative algorithms which alternate image reconstruction and zero-pixels identification (by thresholding or image segmentation) can be considered. However, such brute-force algorithms cannot be implemented efficiently and their convergences are not guaranteed in general. In this paper, we introduce a more sophisticated class of iterative algorithms based on the relatively new concept of so-called sparse signal recovery or compressed sensing〔14〕. The main idea is to include a distance function consisting of ℓ_1 / ℓ_0 norm of reconstructed images into the cost function for image reconstruction. Then, this additional ℓ_1 / ℓ_0 norm term works as a thresholding operation applied after each iteration step, which replaces small pixels values to zeros (i.e. identifying zero-pixels). Here, the word "zero-pixels" refers to pixels which have zero pixel values. As a result, unlike the ordinary iterative algorithms such as ART and EM algorithm, this new class of iterative algorithms can automatically estimate the OS during image reconstruction. When this concept is combined with the EM iterative reconstruction algorithm, it was shown that the resulting algorithm takes the form of alternating the following two substeps 〔15〕. The first substep is the regular iteration step of EM algorithm, and the second substep is the thresholding operation called the hard/soft thresholding in the wavelet literature. The accuracy of zero-pixels identification is improved as the iteration proceeds, and the estimated OS approaches to the exact object boundary.

Recently, such algorithms have been investigated to solve general inverse problems, and are attracting attention of many researchers (e.g. 〔16, 17〕). Our group also applied this class of iterative algorithms to 3D blood vessel reconstruction from limited number of projections 〔18〕 and PET/SPECT reconstruction 〔15〕. In this paper, we use the same concept to estimate the OS in image reconstruction from truncated projection data. As shown later, this concept leads to automatically estimating the OS during the iteration and thereby reducing the DC-shift and low-frequency artifacts significantly.

3) Proposed reconstruction algorithm

In this section, we explain the proposed reconstruction algorithm. First, we note that the iterative algorithm here is essentially same as that in 〔15〕, though the target imaging application and the nature of projection data in this paper are completely different from that in [15]. Let $\vec{x}=(x_1,...,x_n)$ denote the image vector and $\vec{y}=(y_1,...,y_m)$ denote the measured projection data. These two vectors are related to each other by the linear equation $A\vec{x}=\vec{y}$, where $A=\{a_{ij}\}$ is the $m\times n$ system matrix. Then, the proposed cost function for image reconstruction is expressed as

$$f(\vec{x})=L(\vec{x})+\beta T(\vec{x}), \tag{1}$$

Where $L(\vec{x})$ is the negative log-likelihood function, $T(\vec{x})$ is the distance function between the reconstructed image $\vec{x}$ and the null image, and β is the hyperparameter. The definition of $L(\vec{x})$ and $T(\vec{x})$ are given by

$$L(x)=\sum_{i=1}^{m}\left[\sum_{j=1}^{n}a_{ij}x_j-y_i\log\left(\sum_{j=1}^{n}a_{ij}x_j\right)\right] \tag{2}$$

$$T(\vec{x})=\sum_{j=1}^{n}s(x_j),\ \text{and}\ \ s(t)=\lim_{\varepsilon\to+0}|t|^{\varepsilon}\equiv\begin{cases}1 & t\neq 0\\ 0 & t=0\end{cases} \tag{3}$$

We derive the iterative reconstruction algorithm by using the majorization-minimization strategy same as that in [15]. The essential outline of the derivation is as follows. At each iteration k, we approximately majorize the non-separable part of the cost function $L(\vec{x})$ by a separable quadratic function $L(\vec{x};\vec{x}^{(k)})$ around $\vec{x}=\vec{x}^{(k)}$ as:

$$\begin{aligned}L(\vec{x};\vec{x}^{(k)}) &= L(\vec{x}^{(k)})+\nabla L(\vec{x})\,|_{\vec{x}=\vec{x}^{(k)}}\,(\vec{x}-\vec{x}^{(k)})^T+\frac{1}{2}\sum_{j=1}^{n}\frac{\sum_{i=1}^{m}a_{ij}}{x_j^{(k)}}(x_j-x_j^{(k)})^2\\ &=\sum_{j=1}^{n}\frac{\sum_{i=1}^{m}a_{ij}}{2x_j^{(k)}}(x_j-p_j)^2+C(\vec{x}^{(k)})\end{aligned} \tag{4}$$

$$p_j=\frac{x_j^{(k)}}{\sum_{i=1}^{m}a_{ij}}\sum_{i=1}^{m}\frac{a_{ij}y_i}{\sum_{j'=1}^{n}a_{ij'}x_{j'}^{(k)}}\ , \tag{5}$$

where $C(\vec{x}^{(k)})$ is the term independent of $\vec{x}$. Consequently, the final form of the separable surrogate cost function is given by

$$f(\vec{x};\vec{x}^{(k)})=\sum_{j=1}^{n}\beta[t_j(x_j-p_j)^2+s(x_j)]+C(\vec{x}^{(k)})\ \text{with}\ \ t_j=\frac{1}{2\beta x_j^{(k)}}\sum_{i=1}^{m}a_{ij} \tag{6}$$

At each iteration number k, the above cost function $f(\vec{x};\vec{x}^{(k)})$ is minimized instead of $f(\vec{x})$ to obtain the next iterate $\vec{x}^{(k+1)}$. Setting the partial derivative of Eq. (6) with respect to $\vec{x}$ equal to zero and then applying the non-negativity constraint $\vec{x}\geq 0$ yields the iteration formula given below by Eq. (7). The proposed iterative algorithm, which we call Th-OSEM (Threshold ordered subsets expectation maximization), is summarized as follows:

[STEP 1] (Initialization) Set the initial image as $\vec{x}^{(0)}=\varepsilon$ where $\varepsilon>0$ is a small positive number. Set the iteration number as $k\leftarrow 0$.

[STEP 2-1] (Majorization) Around the current iterate $\vec{x}^{(k)}$, $L(\vec{x})$ is (approximately) majorized using the separable function of Eq. (4) to get the surrogate cost function of Eq. (6).

[STEP 2-2] (Minimization) We minimize the cost function of Eq. (6) over $\vec{x}\geq 0$ to obtain the next iteration $\vec{x}^{(k+1)}$:

$$\vec{q}=\arg\min_{\vec{x}} f(\vec{x},\vec{x}^{(k)}),\ \ \vec{x}_j^{(k+1)}=\max(q_j,\delta) \tag{7}$$

where $\delta>0$ is a small value to guarantee that $x^{(k+1)}>0$.

[STEP 3] (Convergence check) Increment the iteration number as $k\leftarrow k+1$ and go to **[STEP 2-1]** until reaching to a stopping criterion.

The practical implementation of the proposed algorithm is simply described as follows. In **[STEP 2-1]**, the majorization substep is applied by computing $\vec{p}=(p_1,p_2,...,p_n)$ using Eq. (5) which is same as executing a single iteration of the conventional OSEM algorithm. The minimization in **[STEP 2-2]** can be explicitly performed by the following thresholding function [15].

$$q_j = \begin{cases} 0 & p_j \le \sqrt{1/t_j} \\ p_j & elsewhere \end{cases}, \tag{8}$$

The Th-OSEM algorithm is executed as one substep of the conventional OSEM algorithm (Eq. (5)) followed by the pixel-by-pixel thresholding (Eq. (8)). The OSEM algorithm was used as a basic iterative algorithm to develop the proposed iterative method, because the non-negativity feature of the EM-based algorithms is helpful in regularizing the solution and estimating the OS more accurately. However, we note that the similar algorithms can be developed based on the other iterative algorithms such as ART and the conjugate gradient. The thresholding function in Eq. (8) has a large similarity to the well-known hard-thresholding operation in the wavelet denoising. This proposed algorithm belongs to a class of recently developed iterative reconstruction algorithms which use a sparsity constraint by employing a distance function based on the ℓ_1 / ℓ_0 norm [15 ~ 18]. A useful theoretical analysis of convergence can be found in [19].

4) Handling the hyperparameter β

In maximum *a posteriori* (MAP) reconstruction algorithms, the hyperparameter β in Eq. (1) is known as the regularization parameter which handles the strength of the prior term. In the proposed algorithm, β controls the size of the thresholding window as in Eq. (8). It is clear that β should be carefully selected, because, if it is assigned to a relatively large value, some low-frequency details in the reconstructed image will be lost due to the strong thresholding. In contrast, if β is relatively small, the merit of thresholding is small and the reconstruction algorithm behaves similar to the conventional iterative algorithms. We propose to use a dynamic value for this parameter by starting with a relatively large value (β_0) and then gradually decreasing it to zero according to the following rule.

$$\lim_{k \to \infty} \beta_k = 0 \quad \text{and} \quad \sum_{k=0}^{\infty} \beta_k = \infty \tag{9}$$

A simple setup to satisfy Eq. (9) is to use $\beta_k = \beta_0 / (1+k)$. This approach is based on the observation that, in the early iterations, a strong thresholding is required for the rough detection of the OS and a weak thresholding is preferred later to retrieve missing image details. We expect that the iteration converges to an approximate solution to the following optimization problem.

$$\text{Minimize } T(\vec{x}) \text{ subject to } A\vec{x} = \vec{y},\ \vec{x} \ge 0 \tag{10}$$

The rationale behind why the dynamic value of hyperparameter β_k should satisfy Eq. (9) is as follows. First, the left equation in Eq. (9) is necessary, because the value of β in the cost function of Eq. (1) should be close to zero for the solution minimizing $f(\vec{x})$ to coincide with the solution to the constrained problem of Eq. (10). On the other hand, the right equation in Eq. (9) intuitively means that the speed to decrease the value of β_k to zero should be sufficiently slow. This constraint is necessary, because, if the speed to decrease the value of β_k is too fast, the iteration is trapped at some point before reaching to the solution minimizing $T(\vec{x})$. For example, $\beta_k = \beta_0 / (1+k)$ satisfies this constraint, but $\beta_k = \beta_0 / (1+k)^2$ does not. We also note that the similar constraints have been used in the row-action maximum likelihood algorithm (RAMLA) for image reconstruction in emission tomography [20] and the gradient descent method with diminishing stepsize [21, p51].

3. Numerical results

1) The effect of OS

Simulation studies were performed to evaluate the effect of *a priori* knowledge of the OS to the quality of reconstructed images. These studies were performed using a single slice (z = 0) of the FORBILD thorax phantom with image matrix size of 512×512 pixels. The ROI was set to be a circle with a diameter of 160 pixels covering the cardiac region as shown in **Fig.** 3(a). The ROI position was selected such that the condition of Defrise is satisfied when the OS is close to the exact one (i.e. the ROI contains a small region outside the exact OS). The projection data were computed with parallel-beam geometry for 512 radial bins and 512 views (over 180°), and the data were truncated manually such that only projection rays passing through the selected ROI are used for the reconstruction. Different selections of the OS constraint μ were applied that include exact OS knowledge, the case where the OS is known with different degrees of OS accuracy (110% ~ 150% larger than the exact OS) and the unknown OS. The "exact OS" means the true exact contour of the scanned object. The "110% OS" means the region inside the ellipse whose semi-axis length is 10% larger than that of the ellipse corresponding to the "exact OS". The definitions of "130% OS" and "150% OS" are similar (see **Fig.** 3(a)). The reconstruction was performed using the conventional OSEM algorithm with 8 subsets and 100 iterations for each setup. The implementation of the iterative reconstruction is as follows:

[Step 1] The image matrix $\vec{x}$ in the iterative algorithm is prepared such that it contains the whole object (not the ROI $\boldsymbol{\Omega}$ only) though only the ROI is the target to be reconstructed accurately.

[Step 2] The whole image matrix $\vec{x}$ is reconstructed by OSEM (section 3.1) or Th-OSEM (section 3.2) using only a set of projection data $\vec{y}$ which intersect the ROI $\boldsymbol{\Omega}$. When the OS is *a priori* known, after every iteration k, pixel values outside the OS are set to zeros.

[Step 3] Trim the reconstructed image matrix $\vec{x}$ to the small image which contains only the ROI $\boldsymbol{\Omega}$.

Reconstructed ROIs are shown in **Fig. 3** and the corresponding ROI central horizontal and vertical profiles are shown in **Fig. 4**. In **Fig. 3**, the reconstructed whole image matrix (512×512 pixels) was trimmed to the ROI image consisting of 512×300 pixels for display. It can be observed that improving the OS accuracy results in reduction of the DC-shift and low-frequency artifacts in the reconstructed images.

We note that, in the problem dealt with in this paper, 100 iterations with 8 subsets are reasonable choices, which were determined from the experimental optimization of iteration number. The explanation is as follows. The OSEM algorithm is normally used in PET/SPECT reconstruction. Though 100 iterations with 8 subsets are too many in PET/SPECT applications, the nature of the reconstruction problem in this paper differs from that in PET/SPECT with respect to the following point. In CT, unlike PET/SPECT imaging, the object normally contains low-contrast structures and the compressed gray scale (e.g. [0.94, 1.03] in **Fig. 3**) is used for image display to make the low-contrast structures visible. To recover the low-contrast structures with allowable small DC/low-contrast artifacts, more numbers of iterations are necessary compared to the case of PET/SPECT. So, we have carefully optimized the iteration number in the experimental study. In **Fig. 5**, we showed the profiles of the reconstructed images with 10, 20, 50,100, and 1000 iterations of the OSEM algorithm with 8 subsets. The results demonstrate that the DC/low-contrast artifacts still continue to decrease up to approximately 100 iterations, but only very small improvements were

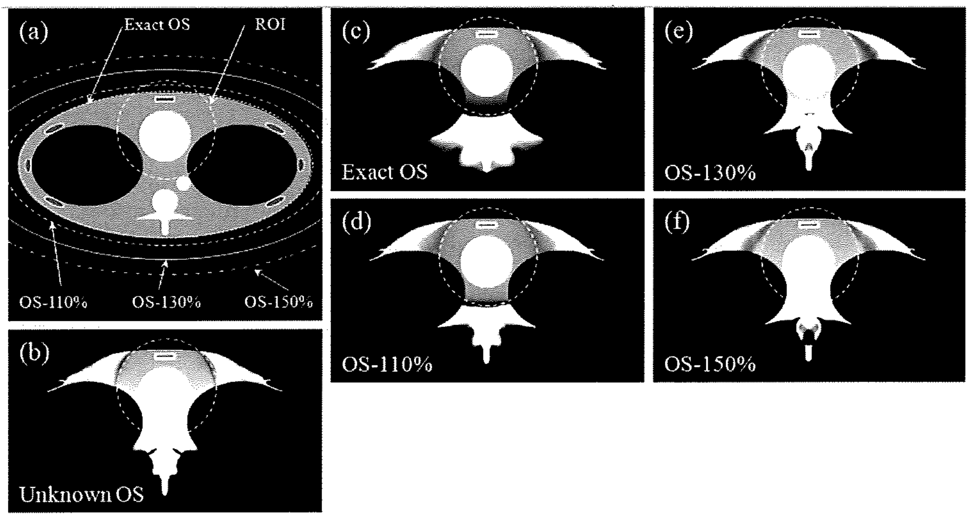

Fig. 3 (a) FORBILD thorax phantom ($z = 0$) and different OS setups, ROI reconstruction results with different OS degrees of accuracy, (b) OS is unknown, (c) OS is exact and (d) ~ (f) OS is known as the region that is larger than the exact OS. The display gray scale is [0.94, 1.03].